

Optimal energy harvesting efficiency from vortex-induced vibration of a circular cylinder under flow

Peng Han^{a,*}, Qiaogao Huang^b, Guang Pan^b, Denghui Qin^b, Wei Wang^c, Rodolfo T. Gonçalves^d, Jisheng Zhao^{e,f,**}

^a*AML, Department of Engineering Mechanics, Tsinghua University, Beijing, 100084, P.R.China*

^b*School of Marine Science and Technology, Northwestern Polytechnical University, Xi'an 710072, P.R.China*

^c*Department of Mechanical Engineering, The Hong Kong Polytechnic University, Hong Kong, China*

^d*Ocean Space Planning Laboratory (OSPL), Department of Systems Innovation, The University of Tokyo, Tokyo 106-0032, Japan*

^e*Fluids Laboratory for Aeronautical and Industrial Research (FLAIR), Department of Mechanical and Aerospace Engineering, Monash University, Clayton 3800, Australia*

^f*School of Engineering and Information Technology, University of New South Wales, Canberra, ACT 102600, Australia*

Abstract

This work applies a combined approach a reduced-order model (ROM) together with experiments and direct numerical simulations to investigate the optimal efficiency of fluid-flow energy harvesting from transverse vortex-induced vibration (VIV) of a circular cylinder. High-resolution efficiency maps were predicted over wide ranges of flow reduced velocities and structural damping ratios, and the maximum efficiency and optimal settings of damping ratio and reduced velocity were then examined for different mass ratios and Reynolds numbers. Efficiencies predicted by the ROM were also validated against either experiments or direct simulations. The present work indicates that: (i) the maximum efficiency is controlled by both the incoming reduced velocity and the product of mass ratio and structural damping ratio, which is similar to the maximum amplitude of VIV; (ii) the maximum efficiency at a relatively high Reynolds number ($Re \approx 6 \times 10^3$) in subcritical regime is higher than that of a low Reynolds number ($Re = 150$) in laminar regime; (iii) the energy harvesting efficiency from VIV of a circular cylinder with a low mass ratio is more robust than that with a high mass ratio. This finding suggests that the VIV harvester performs better in water than in air.

Keywords:

Energy harvesting; Vortex-induced vibration; Reduced-order model; Fluid-structure interactions; Hydrokinetic energy; Water tunnel tests;

*Corresponding author.

**Corresponding author.

Email addresses: hanpeng@mail.tsinghua.edu.cn (Peng Han), Jisheng.Zhao@monash.edu (Jisheng Zhao)

1. Introduction

When an elastic or elastically mounted body is submitted to a transverse flow (for instance, wind or ocean currents), it may vibrate under the fluctuating fluid forces exerted by vortex shedding, and then the body vibration in turn affects the surrounding flow field Païdoussis *et al.* (2010). This typical fluid-structure interaction (FSI) phenomenon is called vortex-induced vibration (VIV). VIV can be widely found in engineering applications and natural lives, such as bridges and buildings (civil engineering), aircraft wings (aerospace engineering), offshore oil risers and mooring lines (ocean engineering), and vibrating leaves and plants in nature Blevins (2001). The circular cylinder has been employed as the standard geometry for investigating VIV, as the circular shape is always symmetrical to the incoming free-stream flow, and the fluid-structure system can therefore be immune to the influence of other instabilities, such as galloping (see Barrero-Gil *et al.*, 2009; Zhao *et al.*, 2014, 2018a). The fundamental research interest and practical importance of flow-induced vibration has motivated a large body of work on modelling, characterising, and predicting the vibration response and vortex shedding modes, well documented in the reviews of Refs (Williamson & Govardhan, 2004; Sarpkaya, 2004) and the books of Refs Païdoussis *et al.* (2010); Blevins (2001).

One of the most important features of VIV is *synchronisation* (also know as “*lock-in*”), where both the vortex shedding frequency and the body vibration frequency are close/equal to the natural frequency, leading to large-amplitude oscillations Williamson & Govardhan (2004). Usually, VIV, particularly in lock-in, is treated as a kind of destructive, high-energy, and harmful phenomenon to the structural safety and thus the primary limiting factor in structural designs, because the structural vibration can potentially lead to structural fatigue and failures Kandasamy *et al.* (2016); Wang *et al.* (2020b). However, in the past decade, researchers have found that the structural vibration can absorb considerable fluid kinetic energy, and thus it is regarded as a promising potential for energy harvesting Bernitsas *et al.* (2008); Rostami & Armandei (2017); Wang *et al.* (2020a, 2021). It has been experimentally and numerically shown that fluid-flow energy harvesting from VIV has many advantages when compared with other conventional techniques such as rotary turbines; for instance, apart from their lower cost to operate and maintain, VIV energy converters can work over a broad range of incoming flow velocities and even at very-low-speed currents, such as rivers and shallow waters Bernitsas *et al.* (2008); Ma *et al.* (2016); Ding *et al.* (2015).

To date, extensive computational fluid dynamics (CFD) and experimental studies have been conducted on enhancing the efficiency of VIV energy harvesters under different structural properties and flow conditions, including the structural damping ratio, surface roughness, and incoming flow velocity (e.g. Ma *et al.*, 2016; Ding *et al.*, 2015; Wang *et al.*, 2019; Soti *et al.*, 2018; Han *et al.*, 2020; Zhao *et al.*, 2022; Lee & Bernitsas, 2011). It has been indicated that the maximum efficiency point always locates within the “lock-in” regime, and it is sensitive to the structural damping, incoming flow velocity, and Reynolds numbers. However, because of the limitations of experimental setup and the high costs of CFD tools,

particularly Direct Numerical Simulation (DNS), it is almost impossible to conduct a detailed optimisation study with a comprehensive parametric space covering wide ranges of the structural properties and fluid conditions. Thus, reduced-order models, with extremely low costs, are effective alternatives to compute and optimise energy conversion efficiency from VIV, despite its less accuracy (see Barrero-Gil *et al.*, 2012; Abdelkefi *et al.*, 2012; Lai *et al.*, 2021).

In this paper, taking the advantages of different research methods for VIV, we present a comprehensive study, by combining a reduced-order model, a quasi-DNS-based FSI solver, and experiments, to better understand and optimise the VIV energy conversion efficiency. We will show that the reduced-order modelling is of cost-efficiency to effectively estimate the peak amplitude response and energy harvesting efficiency of VIV of a circular cylinder, as compared with our direct numerical and experimental results. Of interest, our reduced-order modelling results will show that the global maximum energy harvesting efficiency is barely affected by mass ratio (the ratio of the oscillating mass to the displaced fluid mass) in tested flows. In addition, we will demonstrate that flow reduced velocity and a dimensionless parameter c^* (defined later in §3.1) are the underlying key parameters responsible for the global optimal energy harvesting efficiency.

The rest of the paper is structured as follows. The methodology is introduced in section §2. Then, in section §3, via ROM, the effects of incoming flow velocity, structural damping, and mass ratio on the energy harvesting efficiency, are investigated individually at two Reynolds numbers from the laminar and subcritical regimes. In addition, the optimal efficiency, damping ratio, and reduced velocity will be predicted along with high-resolution maps of the harvesting efficiency. Moreover, the main results obtained by our ROM will be validated against the experiments and direct simulations. Finally, discussions and conclusions are drawn in section §4.

2. Methodology

2.1. Reduced-order model

Figure 1 shows a schematic for the fluid-structure system studied: an elastically mounted rigid circular cylinder is subjected to a free-stream flow, where key parameters are illustrated. With the external fluid force (i.e. the vortex-induced force F_v) exerted by the vortex shedding, the structure system can be modelled by a linear second-order mass-spring-damper oscillator, and the governing equation of motion for the solid cylinder is given by

$$M\ddot{Y} + C\dot{Y} + KY = F_v, \quad (1)$$

where Y , \dot{Y} and \ddot{Y} represent the displacement, velocity, and acceleration, respectively, of the vibrating cylinder. Herein, M represents the total mass including the structural mass M_s and the added mass M_a . For a circular cylinder, the added mass can be calculated by $M_a = C_M \rho D^2 \pi / 4$, where C_M is a coefficient that can be derived from experiments, see §2.3, ρ is the fluid density, and D is the diameter of the cylinder. K represents the spring

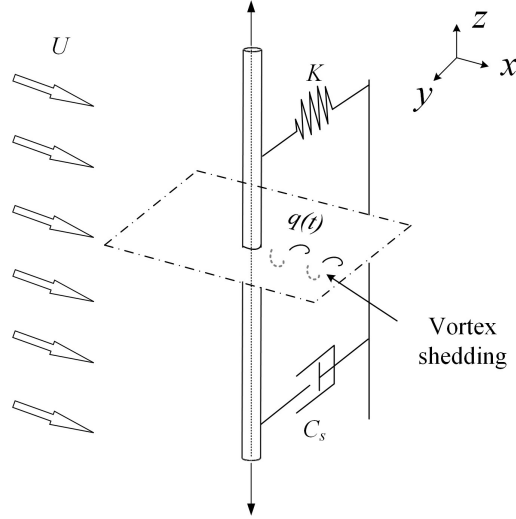


Figure 1: A schematic of the studied problem: an elastically mounted circular cylinder subjected to a free-stream flow, with a representation of the wake oscillator variable $q(t)$.

stiffness; C is the damping factor, and it can be computed by $C = C_s + C_f$, with C_s being the structural damping and C_f being the added damping caused by the fluid loading:

$$C_f = \gamma \omega_f \rho D^2, \quad (2)$$

where γ is a parameter depending on the amplified drag coefficient C_D Blevins (2001); Facchinetti *et al.* (2004):

$$\gamma = C_D / (4\pi St). \quad (3)$$

Note that, the above M , K , C are defined per unit length. In Eq. 2, ω_f is the vortex-shedding angular frequency defined by $\omega_f = 2\pi StU/D$, where St is the Strouhal number for flow over a stationary cylinder, and U is the incoming flow velocity.

Facchinetti *et al.* (2004) proposed a wake oscillator for predicting the vortex-induced lift F_v as follows

$$F_v = \rho U^2 D C_L^v / 2 = \rho U^2 D q C_{L0} / 4, \quad (4)$$

where C_{L0} represents the unsteady lift coefficient of a fixed cylinder. The parameter $q/2$ can be interpreted as a reduced vortex (or “fluctuating”) lift coefficient that represents the ratio between the unsteady vortex-induced lift coefficient of an oscillating cylinder C_L^v and that of the fixed case (C_{L0}) Facchinetti *et al.* (2004); Han & de Langre (2022); Han *et al.* (2021b). The dimensionless wake variable $q(T)$, therefore, directly determines the unsteady lift coefficient caused by vortex shedding, which can be modelled by a van der Pol non-linear wake oscillator equation, following Facchinetti *et al.* (2004):

$$\ddot{q} + \varepsilon \omega_f (q^2 - 1) \dot{q} + \omega_f^2 q = f(Y), \quad f(Y) = (A/D) \ddot{Y}. \quad (5)$$

In this equation, $\varepsilon = 0.3$ and $A = 12$ are constant coefficients derived from experimental data of forced vibrations, see Facchinetti *et al.* (2004); Han *et al.* (2021b). The left-hand side

of the equation is a van der Pol equation with a reference frequency ω_f and a growth rate ε , while the right-hand term, $f(Y)$, is a coupling function of the acceleration \ddot{Y} , connecting the structural dynamics and the wake variable. Now, we introduce some dimensionless terms as follows:

$$\begin{aligned} t &= T\omega_f, & y &= Y/D, & m^* &= 4M_s/\pi\rho D^2, \\ U_r &= 2\pi U/(\omega_s D), & \zeta &= C_s/(2M\omega_s), \end{aligned} \quad (6)$$

where t , y , m^* , U_r , and ζ represent the dimensionless time, dimensionless amplitude, structural mass ratio, reduced velocity, and damping ratio, respectively. Here, ω_s represents the structural angular frequency, defined by $\omega_s = \sqrt{K/M}$. Note that, we use the total mass M instead of the structural mass M_s to define the frequency ω_s and damping ratio ζ . Substituting equation (6) into equations (1)–(5) yields the coupled equations governing the dynamics of the displacement $y(t)$ and the wake variable $q(t)$

$$\ddot{y} + \left(\frac{2\zeta}{U_r S_t} + \frac{4\gamma}{\pi m^* + \pi C_M} \right) \dot{y} + \frac{1}{U_r^2 S_t^2} y = \frac{C_{L0}}{4\pi^3 S_t^2 (m^* + C_M)} \cdot q, \quad (7)$$

$$\ddot{q} + \varepsilon (q^2 - 1) \dot{q} + q = A\ddot{y}. \quad (8)$$

In this paper, the two equations [Eqs. (7)(8)] in ROM are numerically solved using a second-order finite difference scheme in time simultaneously. A small random perturbation on the flow available $q(t)$ is assumed as the initial condition for the numerical method. The simplicity of the reduced-order model, i.e., equations (7) and (8), allows to predict VIV response at extremely low costs. At present, this reduced-order model or its slightly modified forms have been widely and successfully used to predict vortex-induced vibrations under different conditions (e.g., different Re , m^* , ζ , and structural geometry) with qualitative and quantitative agreements (e.g. Facchinetti *et al.*, 2004; Han *et al.*, 2021*b*; Violette *et al.*, 2007, 2010; Zanganeh & Srinil, 2016; Srinil & Zanganeh, 2012).

2.2. Direct Simulation

As mentioned previously in the introduction, computations for the energy harvesting efficiency from VIV at two Reynolds numbers, $Re = 150$ (in laminar regime) and $Re = 6,000$ (in subcritical regime), were performed. To further validate our main results obtained by the proposed reduced-order model, we compared the results with experiments. However, due to the limitations of our experimental setup, it is difficult to conduct VIV tests in ultra low- Re laminar flows, and, to the best of the authors' knowledge, so far there have been no existed published experimental data on energy harvesting in laminar flows. For this reason, we conducted quasi direct numerical simulations on VIV to supplement the validations. The direct simulations was performed by solving the 2D incompressible Navier–Stokes equations for the fluid field and coupling with a mass-spring-damper oscillator similar to equation (1).

The governing equations for the fluid flow, including mass and momentum conservation,

can be written as

$$\nabla \cdot \mathbf{u} = 0 \quad (9)$$

$$\frac{\partial \mathbf{u}}{\partial T} + (\mathbf{u} \cdot \nabla) \mathbf{u} = -\frac{1}{\rho} \nabla p + \nu \nabla^2 \mathbf{u}, \quad (10)$$

where \mathbf{u} , p , and ν represent the velocity field, pressure, and viscosity, respectively. The above equations for the fluid flow are numerically solved by the segregated pressure implicit with splitting of operators algorithm. In addition, we use an implicit first-order scheme for time due to its unconditional stability and a second-order scheme for both the diffusion and convection terms. The structural dynamics coupling with the flow field are solved by the second-order Newmark-beta method, of which the discrete displacement, velocity, and acceleration of the vibration can be respectively written by

$$\ddot{y}_{t+\Delta t} = \frac{1}{\beta_n \Delta t} \left[(y_{t+\Delta t} - y_t) \frac{1}{\Delta t} - \dot{y}_t \right] - \left(\frac{1}{2\beta_n} - 1 \right) \ddot{y}_t \quad (11)$$

$$\dot{y}_{t+\Delta t} = \dot{y}_t + [(1 - \gamma_n) \dot{y}_t + \gamma_n \dot{y}_{t+\Delta t}] \Delta t \quad (12)$$

$$y_{t+\Delta t} = y_t + \dot{y}_t \Delta t + \left[\left(\frac{1}{2} - \beta_n \right) \ddot{y}_t + \beta_n \ddot{y}_{t+\Delta t} \right] \Delta t^2, \quad (13)$$

where $\beta_n = 0.25$ and $\gamma_n = 0.5$ are two constants. More details of the above FSI coupling approaches can be found in the previous studies Han *et al.* (2021a); Han & de Langre (2022); Han *et al.* (2020, 2018).

Figure 2 shows the computational domain used in the numerical simulations, which is of 45D in length and 30D in width. We split the entire domain into seven sub-regions, in order to apply the block dynamic mesh technique. The grids in motion domain (1) are dense and are not updated during the vibration to ensure the numerical accuracy. For more details of the mesh strategy, initial conditions, and boundary conditions, see Han *et al.* (2021a, 2020); Wang *et al.* (2020b).

2.2.1. Validations

So far, the quasi-DNS-based fluid-structure interaction (referred to as DNS-FSI) solver for VIV of a circular cylinder has been developed. In this section, we validate it against published data. Bao *et al.* (2012), Mishra *et al.* (2020), and Zhao (2013) conducted numerical studies of VIV of a circular cylinder with low mass and damping ratios $m^* = 2.546$ and $\zeta = 0$ at $Re = 150$. Using the same parametric settings of m^* , ζ , and Re , we applied our DNS-FSI solver to predict the VIV amplitude response and compared with the previous studies in figure 3. It should be noted that the total grid nodes and dimensionless time step for the present DNS-FSI solver were reasonably set to 10^5 and $\Delta T = 0.002s$ ($\Delta t = 0.01$), considering the results of mesh and time step independence tests. To be consistent with the compared studies, we define the reduced velocity by $U^* = 2\pi U / (D\sqrt{K/M_s})$, without considering the effect of added mass. The validation results in figure 3 show excellent agreements among

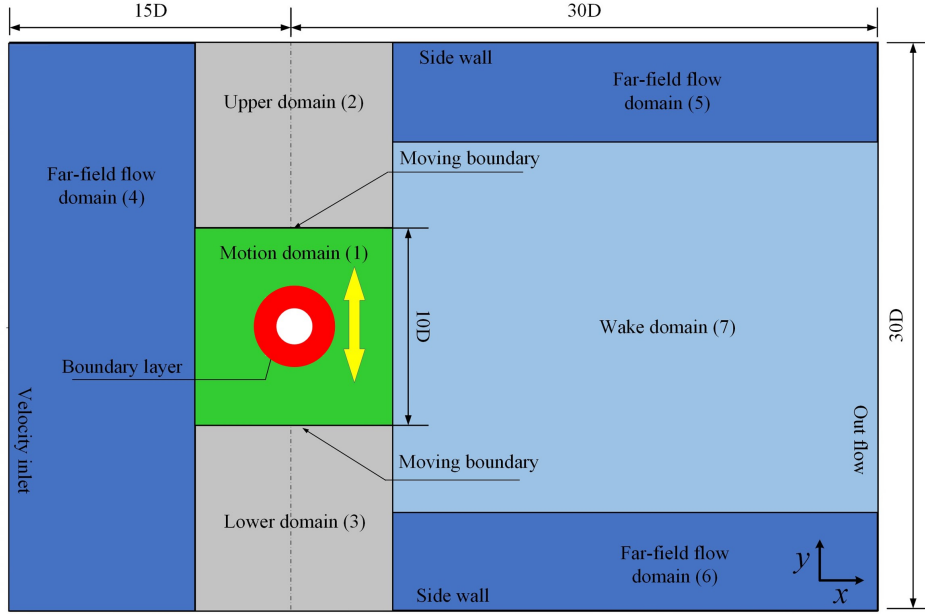


Figure 2: Schematic of the computational domain.

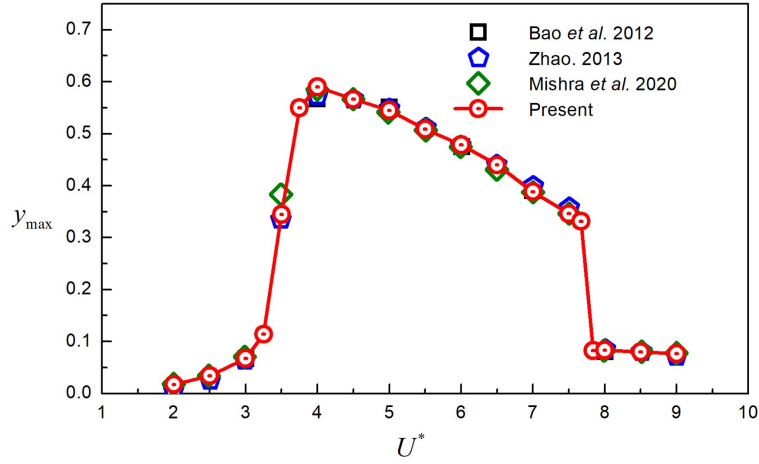


Figure 3: Comparison between the DNS-FSI solver used in the present paper and the previous numerical studies of Bao *et al.* (2012); Mishra *et al.* (2020); Zhao (2013). Parametric settings: $Re = 150$; $m^* = 2.546$; $\zeta = 0$. Here, y_{max} presents the maximum normalised amplitude.

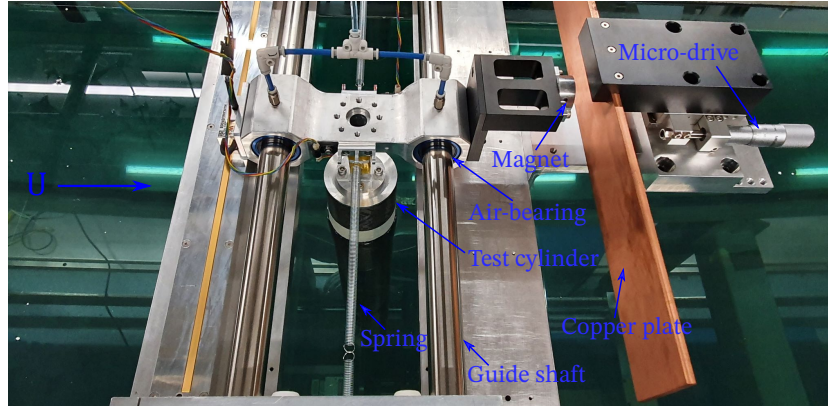


Figure 4: A photograph showing the experimental set-up and its key components.

the present DNS-FSI solver and the previous DNS studies. In addition, we predict the hydrodynamic characteristics of flow over a fixed circular cylinder at $Re = 150$ for further validation, using the proposed DNS-FSI approach without solving the structural dynamics. Table 1 presents the results of the root-mean-square (r.m.s.) of the lift coefficient C_{L0} , the time-averaged drag coefficient C_d , and the Strouhal number St , in comparison with other published studies, confirming again the accuracy of our DNS-FSI solver.

Table 1: A comparison between the preset results and previous published data, of flow over a fixed circular cylinder at $Re = 150$.

Literature	St	Time-averaged C_d	r.m.s. of C_{L0}
Norberg (2003)	0.183	—	0.356
Qu <i>et al.</i> (2013)	0.184	1.305	0.355
Present	0.185	1.331	0.358

2.3. Experimental details

The present experiments were conducted in a recirculating free-surface water channel of the *Fluids Laboratory for Aeronautical and Industrial Research (FLAIR)* at Monash University. This water channel has a test section of 600 mm in width, 800 mm in depth and 4000 mm in length, and the water flow velocity can be varied in the range of $45 \text{ mm/s} \leq U \leq 450 \text{ mm/s}$, with the turbulence level less than 1%. The mass-spring-damper oscillator was modelled on a low-friction air-bearing system. More details and validation studies of the experimental methodologies used can be found in the previous related studies of Zhao *et al.* (2018a); Soti *et al.* (2018); Wong *et al.* (2018).

The test rigid circular cylinder was precision-made to have an outer diameter of $D = 30 \pm 0.01 \text{ mm}$. The immersed length of the cylinder was $L = 614 \text{ mm}$, giving a span-to-diameter ratio (aspect ratio) of 20.5. The displaced mass of fluid (water) was $M_d = \rho \pi D^2 L / 4 = 433.6 \text{ g}$, while the total oscillating mass was $M_s = 2630.6 \text{ g}$, yielding a mass ratio of $m^* = M_s / M_d = 6.07$.

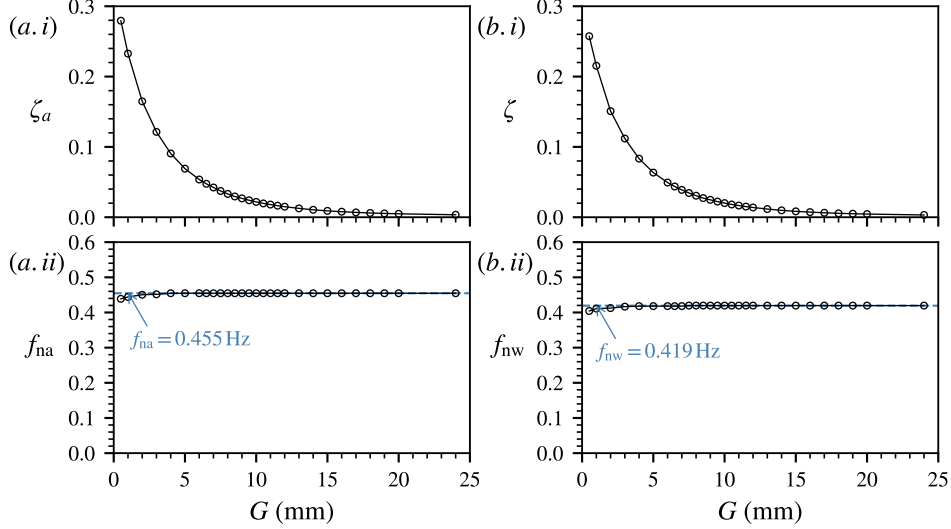


Figure 5: Free decay test results of the structural damping ratios and natural frequencies as a function of the damper gap. Panels (a.i) and (a.ii) show the results of the structural damping ratio (ζ_a) and the natural frequency (f_{na}) in air, respectively, while panels (b.i) and (b.ii) show the structural damping ratio with the consideration of added mass (ζ) and the natural frequency (f_{nw}) in quiescent water, respectively.

To control the structural damping ratio, an eddy-current-based damping device was employed, which consisted of a micro-drive stage with a resolution of 0.01 mm to vary the damper gap for the structural damping control. Photographs of this damping device can be found in the studies of Soti *et al.* (2018); Zhao *et al.* (2022). The structural stiffness of the air-bearing system was given by precision extension springs. Free decay tests were performed to measure the natural frequencies of the mass-spring-damper system: $f_{na} = 0.455$ Hz in air and $f_{nw} = 0.419$ Hz in still waters, while the structural damping ratio with consideration of added mass was given by $\zeta = C/2\sqrt{(K(M_s + M_a))}$, with $M_a = ((f_{na}/f_{nw})^2 - 1)M_s = 471.3$ g and $C_M = M_a/M_d = 1.08$. Figure 5 shows the results of the structural damping ratios and natural frequencies from free decay tests in both quiescent air and water Zhao *et al.* (2022).

3. Results

In this section, we present four high-resolution maps of the energy harvesting efficiency as a function of reduced velocity and damping ratio for different mass ratios and Reynolds numbers. These maps are obtained from our ROM results. Considering the definition of mass ratio in equation (6), for a given VIV energy harvester system, the structural mass M_s is fixed, while the greater the density of the fluid medium ρ the lower the mass ratio m^* is. Thus, two (low and high) mass ratios, $m^* = 6$ and 500, are used to represent as the ocean and wind VIV energy converters, respectively, given the different fluid densities between water and air. Two Reynolds numbers are tested in the present work: the $Re = 150$ case is in the typical laminar regime, while the $Re = 6,000$ case is in the subcritical regime.

Considering one vibration cycle period T_{vib} , the harnessed power by VIV can be computed

by

$$P_h = \frac{1}{T_{vib}} \int_0^{T_{vib}} F_{tot} \frac{dY}{dT} dT = \frac{1}{T_{vib}} \int_0^{T_{vib}} (M_s \frac{d^2Y}{dT^2} + C_s \frac{dY}{dT} + KY) \frac{dY}{dT} dT, \quad (14)$$

where F_{tot} is the total force acting on the vibrating cylinder. Note that the total force can be decomposed by $F_{tot} = F_v - F_a - C_f \dot{Y}$, with F_a is the added-mass forces. In fact, one can find that only the velocity term \dot{Y} can contribute to the harnessed power, while the other terms that related to the \ddot{Y} and Y will become zero after integration (see Soti *et al.*, 2018; Han *et al.*, 2020). Thus, equation (14) can be rewritten by

$$P_h = \int_0^{T_{vib}} \frac{1}{T_{vib}} (C_s \frac{dY}{dT}) \frac{dY}{dT} dT = \left\langle C_s \left(\frac{dY}{dT} \right)^2 \right\rangle, \quad (15)$$

where $\langle \cdot \rangle$ represents the time-averaged operation. To estimate the energy harvesting efficiency, we introduce the power produced by the fluid flow:

$$P_f = \frac{1}{2} \rho U^3 (D), \quad (16)$$

Note that, there are in fact several criteria to define P_f , depending on using D or $D + 2y_{max}$, as the projected area (see for instance Bernitsas *et al.* (2008); Grouthier *et al.* (2014); Ding *et al.* (2015)). A different definition of P_f will not affect the results, while it is only related to the data post-processing. Here, we use the same definition as in Refs Ding *et al.* (2015); Grouthier *et al.* (2014) and our previous studies Soti *et al.* (2018); Han *et al.* (2021a); Zhao *et al.* (2022) for consistency. Now, the efficiency η can be defined as the ratio of the harnessed power to the fluid power available, namely $\eta = P_h/P_f$. By substituting the dimensionless time t , damping ratio ζ , dimensionless amplitude y , mass ratio m^* , and reduced velocity U_r into the equation for η , it gives

$$\eta = \frac{8\pi^4 St^2 (m^* + C_M) \langle \zeta \dot{y} \dot{y} \rangle}{U_r}. \quad (17)$$

3.1. Energy harvesting from VIV at high- Re in the subcritical regime

As can be seen from equations (15) and (17), the energy harvesting efficiency η is strongly determined by the damping ratio ζ , reduced velocity U_r and mass ratio m^* . For a given VIV energy harvester, the structural mass ratio is generally fixed, while the other two terms may vary. Here, we apply the reduced-order model to optimise the efficiency as a function of U_r and ζ , individually at a high mass ratio $m^* = 500$ (for wind VIV energy converter) and a low mass ratio $m^* = 6$ (for ocean energy converter). The tested Reynolds number is around 6×10^3 . The flow parameters, i.e., the lift coefficient $C_{L0} = 0.7$ and Strouhal number $St = 0.208$ of flow over a fixed cylinder, used for our ROM are taken from experiments under the same Reynolds number Norberg (2003); Zhao *et al.* (2018b). Figure 6 shows the full efficiency map spanning the reduced velocity range $0.3 \leq U_r \leq 15$ and the damping ratio range $0.0001 \leq \zeta \leq 10$, at $m^* = 6$. Both the ranges of U_r and ζ are wide enough to cover the high-efficiency region, while the efficiency outside the computed space is negligible. The results

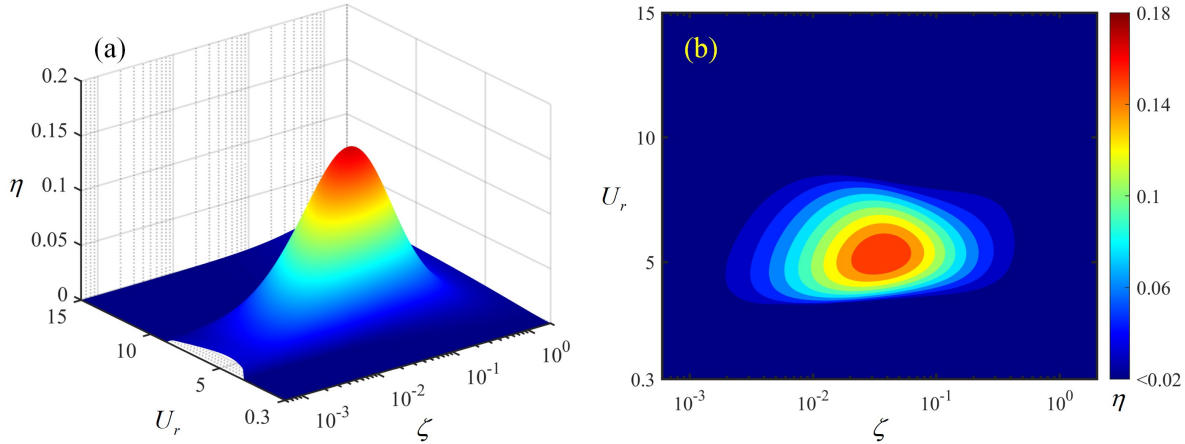


Figure 6: Contour maps of the energy harvesting efficiency η as a function of the reduced velocity U_r and damping ratio ζ , at $m^* = 6.07$ and $Re \approx 6 \times 10^3$. The right plot shows the contour map of the left one in a two-dimensional plane.

in figure 6 indicate that η first increases and then experiences a decrease with increasing U_r . A comparable scenario can be found for the effects of damping ratio on the efficiency. Overall, the maximum efficiency is found to be $\eta \approx 0.17$, while, correspondingly, the optimal reduced velocity and damping ratio are $U_r = 5.275$ and $\zeta = 0.0379$, respectively. One can find that the optimal U_r is slightly higher than the resonance velocity $1/St$, indicating the maximum efficiency locates among the lock-in range, consistent with the previous studies of RefsBernitsas *et al.* (2008); Soti *et al.* (2018).

To further validate our predicted results obtained by the ROM, we conducted experiments on VIV of a circular cylinder under the same flow conditions and structural parameters as numerical predictions. First, to validate the ROM results for the effect of velocity U_r , the damping ratio was kept unchanged at $\zeta = 0.0305$ near the optimal value, while the reduced velocity U_r was varied from 2.8 to 14. Figure 7(a) shows a comparison of η obtained from our experiments and ROM. It can be seen that our ROM can capture the maximum efficiency, the resonance phenomenon, and most features due to the influence of reduced velocity. More specifically, the value of maximum efficiency predicted by ROM is 0.164, observed at $\zeta = 0.0305$, which is highly close to the experimental value 0.173. Also, the optimal reduced velocity in figure 7(a) obtained by our ROM and experiments are similar, i.e., $U_r = 5.3$ for ROM and $U_r = 5.6$ for experiments. Second, keeping the reduced velocity U_r fixed at 5.5 near the optimal value, we compare the effect of damping ratio predicted by the ROM and that obtained from our experiments in figure 7(b). The experimental results show the maximum efficiency 0.173 occurring at $\zeta = 0.03445$ and 0.0388, while the ROM sees the predicted maximum efficiency $\eta = 0.164$ and the optimal damping ratio $\zeta = 0.0383$ in excellent agreement with the experiments. However, some differences can still be found between our ROM and experiments. This is mainly because the body oscillation is not perfectly in phase with the acceleration, particularly for a low-mass-ratio body in the VIV lower branch (see Williamson & Govardhan, 2004; de Langre, 2006). Thus, the proposed

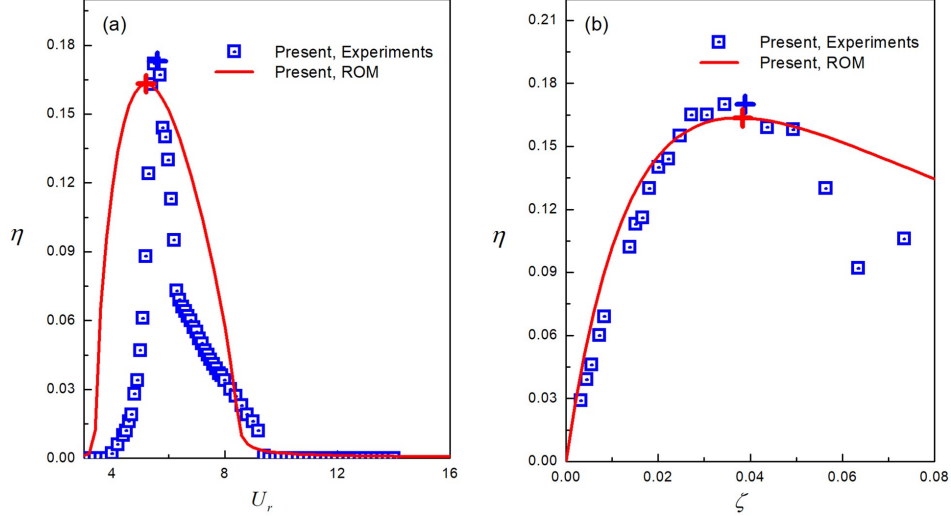


Figure 7: Comparisons of the variations of energy harvesting efficiency η as a function of the (a) reduced velocity U_r and (b) damping ratio ζ , obtained by our ROM and experiments. ”+” presents the maximum efficiency point.

ROM, coupling with the body acceleration \ddot{y} [see equation (8)], cannot capture the classical lower branch of VIV Facchinetti *et al.* (2004), which leads to some discrepancies on the phase angle prediction. Perhaps, introducing an out-of-phase term (i.e., the velocity \dot{y}) coupled with the acceleration term \ddot{y} in equation (8) may improve the accuracy for the predictions of phase and thus the amplitude and efficiency; however, this would make the ROM become more complicated, which is beyond the scope of present study. In addition, more accurate fits with the experimental results could probably be obtained if the coefficients used in our ROM were modified. This would not be illegitimate as, for instance, the lift coefficient C_{L0} and Strouhal numbers St have been found to vary over certain ranges – for more details, see the review study of Norberg (2003). A sensitive analysis of the parameters C_{L0} and St on the ROM has been reported in the recent work of Han & de Langre (2022). In general, by comparing with present experiments, we can conclude that the proposed ROM, with extremely low costs, can qualitatively and to some extent quantitatively predict the energy harvesting efficiency from the complex FSI phenomenon – vortex-induced vibration.

In terms of the high-mass-ratio oscillator (i.e., to represent the wind VIV energy harvester), figure 8 presents a full map of the efficiency predicted using the ROM. In this case, the applied parameters remain the same as in figure 6, except $m^* = 500$. The results show that the peak value of efficiency $\eta = 0.17$ is barely affected by the mass ratio. The optimal reduced velocity and damping ratio for this mass ratio are found to be 5.25 and 5.168×10^{-4} , respectively. The optimal reduced velocities U_r for the two mass ratio cases tested are almost the same, which are close to the resonance velocity. It is interesting to note that the optimal damping ratio for the low-mass-ratio case in figure 6 is approximately 73 times of that of the high-mass-ratio case. Moreover, considering the effect of added mass, the two mass ratio cases tested, i.e., $6 + 1.08$ and $500 + 1.08$, also differ similarly by a factor of 71.

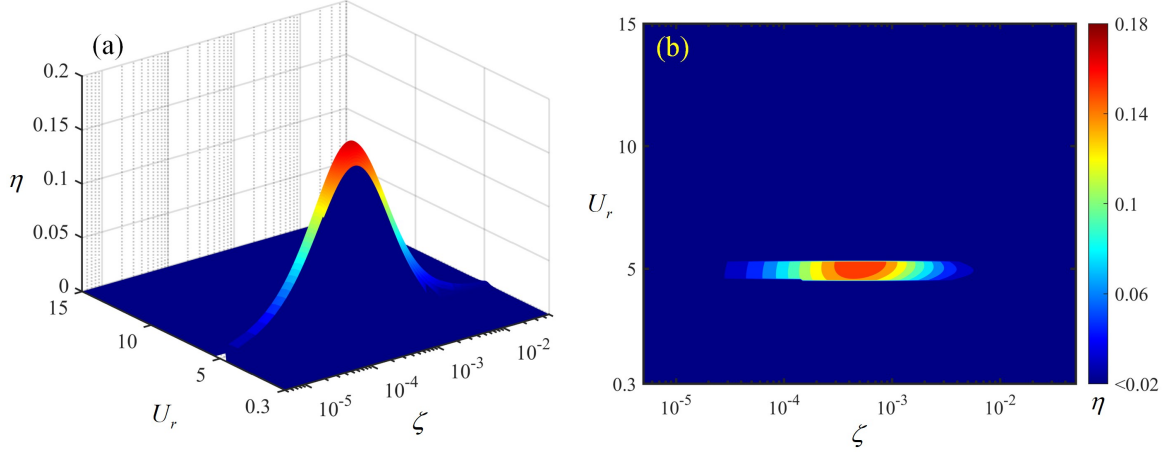


Figure 8: Contour maps of the energy harvesting efficiency η as a function of the reduced velocity U_r and damping ratio ζ , at $m^* = 500$ and $Re \approx 6 \times 10^3$. The right plot shows the contour map of the left one in a two-dimensional plane

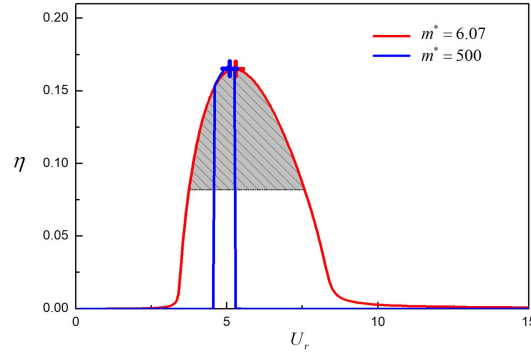


Figure 9: Comparison of the energy harvesting efficiency η as a function of U_r at the optimal damping ratio between a low and a high mass ratio. The + symbols represent the locations of the maximum efficiency for each mass ratio case.

This seems to suggest that the location of the maximum efficiency point η is controlled by the reduced velocity and the product of the total mass and damping ratios $(m^* + C_M)\zeta$. In fact, the coupled mass-damping parameters or its modified forms (such as Skop-Griffin parameter S_G and Scruton number S_c) are known to determine the peak amplitude of VIV Blevins (2001); Williamson & Govardhan (2004). However, as reported by Vandiver (2012), the parameter $(m^* + C_M)\zeta$ also has its limitations. Vandiver (2012) derived a parameter c^* , namely $c^* = 2C_s\omega_v/\rho U^2$ (ω_v is the angular frequency of vibrations), to replace the coupled mass-damping parameter to collapse the VIV amplitudes. Following Vandiver (2012), we here show that the parameter c^* can be useful to control the maximum energy harvesting efficiency point as well. The parameters c^* for the global optimal efficiency are identical for both the two mass ratios: it is 1.14 for $m^* = 6$ and 1.16 for $m^* = 500$. More details and analysis on this are given in section §4.

To better compare the energy harvesting performance at low and high mass ratios, figure 9

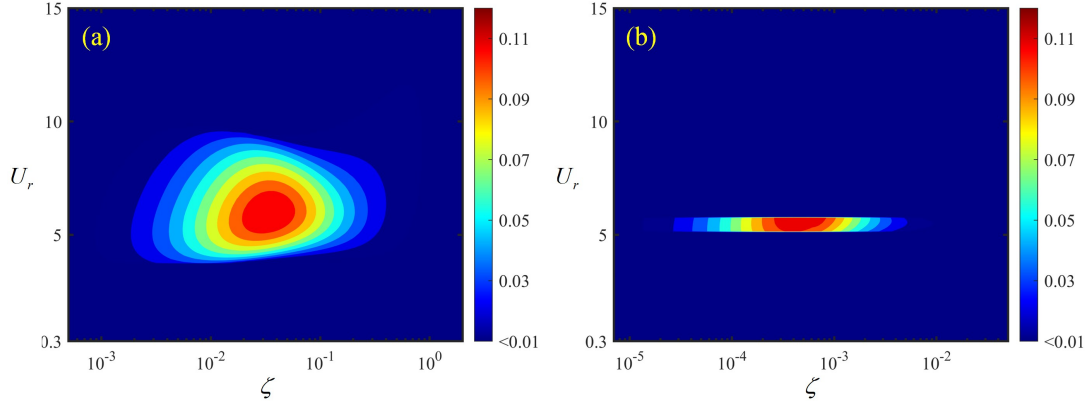


Figure 10: Optimisation of the energy harvesting efficiency η as a function of U_r and ζ in a low-Re flow at (a) $m^* = 6.07$ and (b) $m^* = 500$.

shows the variation of η with U_r at the optimal damping ratios for $m^* = 6$ and 500. Note that, as mentioned previously in Section 2.1, the present paper uses a small random perturbation on the $q(t)$ as the initial condition to start the ROM computations, assuming the structural body vibrates from rest. Actually, a different initial condition (small/large/increasing velocity/decreasing velocity perturbations on the system) will give the different predictions for a high-mass system, mainly because of inertia effects. A large perturbation or increasing velocity initial conditions on the FSI system, particularly a high-mass-ratio system, allow to yield a wide range of lock-in, but the maximum efficiency point is still the same as the predictions with a small perturbation. The effect of the initial conditions however is out of the scope of the present paper and will not be discussed in detail. Here, we define the high-efficiency region among which the efficiency η is larger than the half of the maximum value observed. As can be seen, although the maximum efficiency is almost identical for the two mass ratios, the high-efficiency regime for the case of $m^* = 6$ is obviously wider than that of $m^* = 500$. This phenomenon is attributable to the fact that the lock-in (or synchronisation) range, where significant energy harvesting performance is achieved, for the low-mass-ratio case is much wider than that of the high-mass-ratio case. Note that a lighter body can enhance the fluid-structure interaction and thus the wake instabilities responsible for the cause of the structural vibration (see de Langre, 2006). By comparing the results in figures 6, 8, and 9, it can be concluded that the energy harvesting efficiency is more robust for a low-mass-ratio system, indicating that VIV energy harvesters should perform better in water than in air.

3.2. Energy harvesting from VIV in a laminar flow

In this section, we investigate the characteristics of the energy harvesting efficiency from VIV in a laminar flow. Using the parameters $C_{L0}^{r.m.s.} = 0.36$ and $S_t = 0.185$ taken from table 1 for flow over a fixed circular cylinder at $Re = 150$, we construct the full energy harvesting efficiency maps for the two mass ratios, $m^* = 6$ and 500, in a laminar flow. As can be seen in figure 10, similar effects of U_r , ζ , and m^* on the efficiency are observed for two mass ratio cases at $Re = 150$ (figures 6 and 8). For $m^* = 6$ in figure 10(a), the maximum

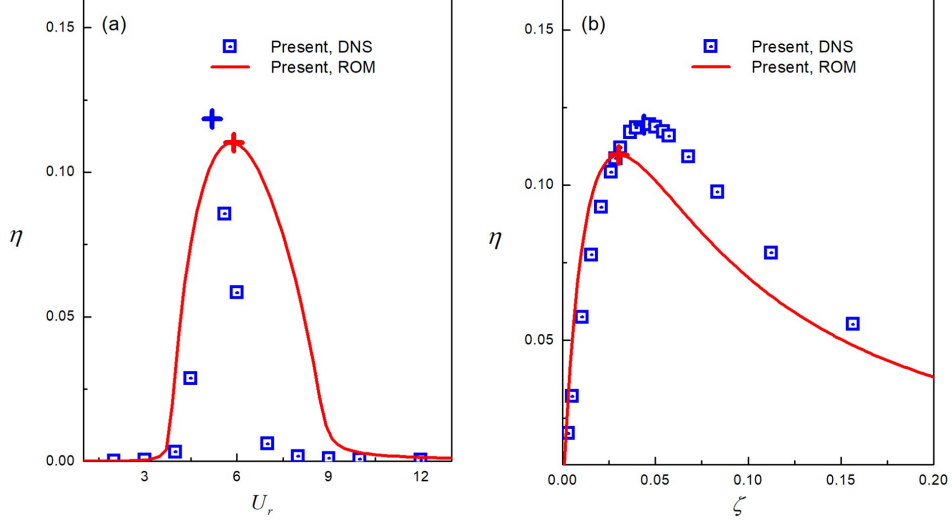


Figure 11: Comparisons of the variations of energy harvesting efficiency η as a function of the (a) reduced velocity U_r and (b) damping ratio ζ , obtained by our ROM and quasi direct numerical simulations. ”+” presents the maximum efficiency point.

efficiency is observed to be 0.118, occurring at $U_r = 5.92$ and $\zeta = 0.0338$. On the other hand, for $m^* = 500$ in figure 10(b), the maximum efficiency is found to be $\eta = 0.119$ and the optimal velocity $U_r = 5.90$, similar to the case of $m^* = 6$, while the optimal damping ratio is 70 times lower than that of the case of $m^* = 6$. Note that the product of the optimal damping ratio and the total mass ratio is found to be 0.239 and 0.241 for $m^* = 6$ and 500, respectively. The parameter c^* for the heavy ($m^* = 500$) and light ($m^* = 6$) FSI systems at the optimal efficiency points are 0.83 and 0.84, respectively. The above two nearly identical values indicate that the maximum energy harvesting efficiency is predominantly controlled by c^* , regardless of the present tested two Reynolds numbers. Comprehensively from the results in figures 6, 8 and 10, in general, the overall performance of energy harvesting from VIV at $Re = 6,000$ from the subcritical regime is better than that at $Re = 150$ from the laminar regime.

In order to further support the results obtained by our ROM, we validate them against the numerical data predicted by our DNS-FSI solver. Figure 11 shows the predicted η as a function of U_r in (a) and ζ in (b). Note that in figure 11(a), the damping ratio is fixed at $\zeta = 0.044$, while in figure 11(b) the reduced velocity is fixed at $U_r = 5.2$. Qualitative and to some extent quantitative agreements can be found between our ROM and DNS results in terms of the maximum efficiency locations, as well as the effects of U_r and ζ . In addition, the maximum η values predicted by our ROM and DNS-FSI tests agree well with the numerical simulations by Soti *et al.* (2017) who showed a maximum η value of 0.13.

4. Discussions

From figures 6, 8 and 10, it is found that although the energy harvesting characteristics for a heavy ($m^* = 500$) and light ($m^* = 6$) VIV systems under flow are distinctly differ-

ent, the global maximum efficiency points are identical, regardless two different Reynolds numbers in the present study. In addition, the parameter $c^* = 2C_s\omega_v/\rho U^2$ for the global optimal efficiency point was found to be also nearly identical. The above findings are further confirmed through the comparisons of the optimal efficiency η_{max} respect to the c^* under different mass ratios and Reynolds numbers, as shown in figure 12. The comparisons support that not only the global optimal efficiency but also the maximum efficiency under each damping ratio ζ are governed by c^* number. Interestingly, many previous studies focusing on the effect of c^* or combined mass-damping parameter on the maximum amplitude of VIV have indicated that the maximum amplitude can be expressed as a function of the related controlled parameter by some empirical parameters (e.g. Williamson & Govardhan, 2004; Soti *et al.*, 2018), or more importantly by linearised reduced-order models (e.g. Facchinetti *et al.*, 2004). This is interesting, because the underlying relationship between the maximum amplitude and the efficiency shows a certain way for future work to simplify the relationship by linearising our ROM to describe the optimal energy harvesting efficiency from VIV.

As can be seen again from figures 6, 8 and 10, the optimal energy harvesting efficiency is strongly related to Reynolds number, indicating that the VIV energy harvester performs better in a subcritical flow than that in a laminar flow. The results agrees well with the findings from previous studies that the energy harvesting efficiency tends to increase with Reynolds number. For example, the numerical results of Soti *et al.* (2017) reported the energy harvesting efficiency to be 0.10, 0.13 and 0.145 for $Re = 100, 150$ and 200 , respectively, while the experimental results of Soti *et al.* (2018) showed that the efficiency can be varied from 0.151 to 0.200 for $10^3 < Re < 10^4$. From their experiments at $Re \approx 7.5 \times 10^4$, Lee & Bernitsas (2011) reported a maximum efficiency about 0.33. However, from the perspective of computations of our proposed ROM, the differences between low- and high- Re cases are related to the lift coefficient (C_{L0}) and Strouhal number (St) of flow over a fixed circular cylinder. According to Norberg (2003), C_{L0} and St do not monotonically vary with Re ; thus, the efficiency may not always increase with Re as an optimal Reynolds number would be expected to occur with a large C_{L0} and an appropriate St . Further investigations on this would be warranted.

5. Conclusions

We have applied a combined approach based on a reduced-order model, a DNS-FSI solver, and experiments to investigate the optimal efficiency of fluid-flow energy harvesting from VIV of a circular cylinder over a wide parametric space of reduced velocity and structural damping ratio. Based on the results, conclusions from the present work are drawn below.

The maximum efficiency and the optimal settings of damping ratio and reduced velocity under different conditions were successfully predicted by the reduced-order model and validated against either our experiments and quasi-DNS. This indicates that the ROM is an low-cost tool for optimization of efficiency and it is valuable for related engineering designs. Moreover, via ROM, it shows that the maximum energy harvesting efficiency is strongly controlled by a dimensionless damping-mass parameter c^* and the reduced velocity U_r .

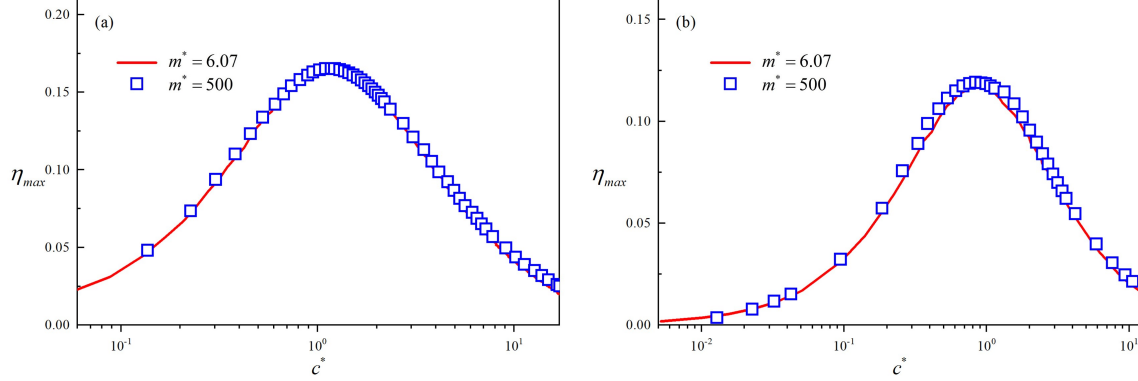


Figure 12: The variations of optimal energy harvesting efficiency as a function of the dimensionless parameter c^* at (a) $Re = 6,000$ and (b) $Re = 150$.

A VIV-energy converter works better in a subcritical flow than that in a laminar flow. Combing the present results and those in literature, it seems that a high Re would lead to a better efficiency in terms of energy harvesting. However, from the mechanics among the present reduced-order model, a large C_{L0} and an appropriate St are the key parameters affecting the efficiency and therefore an optimal Re is expected. Further investigations on this would be warranted.

As it has been shown in the present work, a low-mass-ratio VIV energy harvester performs better than a high-mass-ratio system, indicating that an ocean energy harvester has more potential in fluid power conversion than that of a wind energy harvester. This fact is because the mass ratio effect plays an important role affecting the dynamics in the lock-in region. As it has been reported in the literature (e.g. Williamson & Govardhan, 2004), the circular cylinder with an extremely low mass ratio may undergo high-amplitude VIV over a larger range of reduced velocities, even to an infinite reduced velocity (achieved by setting $K = 0$); thus, it would be of great interest to combine reduced-reduced modelling and experimental approaches to further investigate the energy harvesting performance from VIV of an extremely-low-mass-ratio body and, of course, other flow-induced vibration systems.

Acknowledgement

This work was supported by the Australian Research Council through a Discovery Early Career Researcher Award (DE200101650, J.Z.).

References

ABDELKEFI, A., HAJJ, M. R. & NAYFEH, A. H. 2012 Phenomena and modeling of piezoelectric energy harvesting from freely oscillating cylinders. *Nonlinear Dynamics* **70** (2), 1377–1388.

- BAO, YAN, HUANG, CHENG, ZHOU, DAI, TU, JIAHUANG & HAN, ZHAOLONG 2012 Two-degree-of-freedom flow-induced vibrations on isolated and tandem cylinders with varying natural frequency ratios. *Journal of Fluids and Structures* **35**, 50–75.
- BARRERO-GIL, ANTONIO, PINDADO, SANTIAGO & AVILA, SERGIO 2012 Extracting energy from vortex-induced vibrations: A parametric study. *Applied Mathematical Modelling* **36** (7), 3153–3160.
- BARRERO-GIL, A., SANZ-ANDRÉS, A. & ALONSO, G. 2009 Hysteresis in transverse galloping: The role of the inflection points. *Journal of Fluids and Structures* **25** (6), 1007–1020.
- BERNITSAS, MICHAEL M., RAGHAVAN, KAMALDEV, BEN-SIMON, Y. & GARCIA, E. M. 2008 VIVACE (Vortex Induced Vibration Aquatic Clean Energy): A new concept in generation of clean and renewable energy from fluid flow. *Journal of Offshore Mechanics and Arctic Engineering* **130** (4), 041101–041101–15.
- BLEVINS, ROBERT D. 2001 *Flow-Induced Vibration*. Krieger Publishing Company.
- DING, LIN, ZHANG, LI, WU, CHUNMEI, MAO, XINRU & JIANG, DEYI 2015 Flow induced motion and energy harvesting of bluff bodies with different cross sections. *Energy Conversion and Management* **91**, 416–426.
- FACCHINETTI, M. L., DE LANGRE, E. & BIOLLEY, F. 2004 Coupling of structure and wake oscillators in vortex-induced vibrations. *Journal of Fluids and Structures* **19** (2), 123–140.
- GROUTHIER, CLÉMENT, MICHELIN, SÉBASTIEN, BOURGUET, RÉMI, MODARRES-SADEGHI, YAHYA & DE LANGRE, EMMANUEL 2014 On the efficiency of energy harvesting using vortex-induced vibrations of cables. *Journal of Fluids and Structures* **49**, 427–440.
- HAN, PENG, HUANG, QIAOGAO, PAN, GUANG, WANG, WEI, ZHANG, TIANQI & QIN, DENGHUI 2021*a* Energy harvesting from flow-induced vibration of a low-mass square cylinder with different incidence angles. *AIP Advances* **11** (2), 025126.
- HAN, PENG, HÉMON, PASCAL, PAN, GUANG & DE LANGRE, EMMANUEL 2021*b* Nonlinear modeling of combined galloping and vortex-induced vibration of square sections under flow. *Nonlinear Dynamics* **103** (4), 3113–3125.
- HAN, PENG & DE LANGRE, EMMANUEL 2022 There is no critical mass ratio for galloping of a square cylinder under flow. *Journal of Fluid Mechanics* **931**, A27.
- HAN, PENG, PAN, GUANG & TIAN, WENLONG 2018 Numerical simulation of flow-induced motion of three rigidly coupled cylinders in equilateral-triangle arrangement. *Physics of Fluids* **30** (12), 125107.

- HAN, PENG, PAN, GUANG, ZHANG, BAOSHOU, WANG, WEI & TIAN, WENLONG 2020 Three-cylinder oscillator under flow: Flow induced vibration and energy harvesting. *Ocean Engineering* **211**, 107619.
- KANDASAMY, RAMKUMAR, CUI, FANGSEN, TOWNSEND, NICHOLAS, FOO, CHOON CHI-ANG, GUO, JUNYAN, SHENOI, AJIT & XIONG, YEPING 2016 A review of vibration control methods for marine offshore structures. *Ocean Engineering* **127**, 279–297.
- LAI, ZHIHUI, WANG, SHUAIBO, ZHU, LIKUAN, ZHANG, GUOQING, WANG, JUNLEI, YANG, KAI & YURCHENKO, DANIIL 2021 A hybrid piezo-dielectric wind energy harvester for high-performance vortex-induced vibration energy harvesting. *Mechanical Systems and Signal Processing* **150**, 107212.
- DE LANGRE, E. 2006 Frequency lock-in is caused by coupled-mode flutter. *Journal of Fluids and Structures* **22** (6-7), 783–791.
- LEE, J. H. & BERNITSAS, M. M. 2011 High-damping, high-Reynolds VIV tests for energy harnessing using the VIVACE converter. *Ocean Engineering* **38** (16), 1697–1712.
- MA, CHUNHUI, SUN, HAI, NOWAKOWSKI, GARY, MAUER, ERIK & BERNITSAS, MICHAEL M. 2016 Nonlinear piecewise restoring force in hydrokinetic power conversion using flow induced motions of single cylinder. *Ocean Engineering* **128**, 1–12.
- MISHRA, RAHUL, SOTI, ATUL, BHARDWAJ, RAJNEESH, KULKARNI, SALIL S. & THOMPSON, MARK C. 2020 Transverse vortex-induced vibration of a circular cylinder on a viscoelastic support at low reynolds number. *Journal of Fluids and Structures* **95**, 102997.
- NORBERG, C. 2003 Fluctuating lift on a circular cylinder: review and new measurements. *Journal of Fluids and Structures* **17** (1), 57–96.
- PAÏDOUSSIS, MICHAEL P., PRICE, STUART J. & DE LANGRE, EMMANUEL 2010 *Fluid-Structure Interactions: Cross-Flow-Induced Instabilities*. Cambridge University Press.
- QU, LIXIA, NORBERG, CHRISTOFFER, DAVIDSON, LARS, PENG, SHIA-HUI & WANG, FUJUN 2013 Quantitative numerical analysis of flow past a circular cylinder at reynolds number between 50 and 200. *Journal of Fluids and Structures* **39**, 347–370.
- ROSTAMI, ALI BAKHSHANDEH & ARMANDEI, MOHAMMADMEHDI 2017 Renewable energy harvesting by vortex-induced motions: Review and benchmarking of technologies. *Renewable and Sustainable Energy Reviews* **70**, 193–214.
- SARPKAYA, T. 2004 A critical review of the intrinsic nature of vortex-induced vibrations. *Journal of Fluids and Structures* **19** (4), 389–447.
- SOTI, ATUL KUMAR, THOMPSON, MARK C., SHERIDAN, JOHN & BHARDWAJ, RAJNEESH 2017 Harnessing electrical power from vortex-induced vibration of a circular cylinder. *Journal of Fluids and Structures* **70**, 360–373.

- SOTI, A. K., ZHAO, J. S., THOMPSON, M. C., SHERIDAN, J. & BHARDWAJ, R. 2018 Damping effects on vortex-induced vibration of a circular cylinder and implications for power extraction. *Journal of Fluids and Structures* **81**, 289–308.
- SRINIL, NARAKORN & ZANGANEH, HOSSEIN 2012 Modelling of coupled cross-flow/in-line vortex-induced vibrations using double Duffing and van der Pol oscillators. *Ocean Engineering* **53**, 83–97.
- VANDIVER, J. KIM 2012 Damping parameters for flow-induced vibration. *Journal of Fluids and Structures* **35**, 105–119.
- VIOLETTE, R., DE LANGRE, E. & SZYDLOWSKI, J. 2007 Computation of vortex-induced vibrations of long structures using a wake oscillator model: Comparison with DNS and experiments. *Computers and Structures* **85** (11-14), 1134–1141.
- VIOLETTE, R., DE LANGRE, E. & SZYDLOWSKI, J. 2010 A linear stability approach to vortex-induced vibrations and waves. *Journal of Fluids and Structures* **26** (3), 442–466.
- WANG, JUNLEI, GENG, LINFENG, DING, LIN, ZHU, HONGJUN & YURCHENKO, DANIL 2020a The state-of-the-art review on energy harvesting from flow-induced vibrations. *Applied Energy* **267**, 114902.
- WANG, JUNLEI, YURCHENKO, DANIL, HU, GUOBIAO, ZHAO, LIYA, TANG, LIHUA & YANG, YAOWEN 2021 Perspectives in flow-induced vibration energy harvesting. *Applied Physics Letters* **119** (10).
- WANG, JUNLEI, ZHOU, SHENGXI, ZHANG, ZHIEN & YURCHENKO, DANIL 2019 High-performance piezoelectric wind energy harvester with Y-shaped attachments. *Energy Conversion and Management* **181**, 645–652.
- WANG, WEI, SONG, BAOWEI, MAO, ZHAOYONG, TIAN, WENLONG, ZHANG, TINGYING & HAN, PENG 2020b Numerical investigation on vortex-induced vibration of bluff bodies with different rear edges. *Ocean Engineering* **197**, 106871.
- WILLIAMSON, C. H. K. & GOVARDHAN, R. 2004 Vortex-induced vibrations. *Annual Review of Fluid Mechanics* **36** (1), 413–455.
- WONG, K. W. L., ZHAO, J., LO JACONO, D., THOMPSON, M. C. & SHERIDAN, J. 2018 Experimental investigation of flow-induced vibration of a sinusoidally rotating circular cylinder. *Journal of Fluid Mechanics* **848**, 430–466.
- ZANGANEH, HOSSEIN & SRINIL, NARAKORN 2016 Three-dimensional VIV prediction model for a long flexible cylinder with axial dynamics and mean drag magnifications. *Journal of Fluids and Structures* **66**, 127–146.

- ZHAO, J., HOURIGAN, K. & THOMPSON, M. C. 2018*a* Flow-induced vibration of D-section cylinders: an afterbody is not essential for vortex-induced vibration. *Journal of Fluid Mechanics* **851**, 317–343.
- ZHAO, J., HOURIGAN, K. & THOMPSON, M. C. 2022 Damping effect on transverse flow-induced vibration of a rotating circular cylinder and its implied energy harvesting performance. *Physical Review Fluids* **7**.
- ZHAO, J., LEONTINI, J. S., LO JACONO, D. & SHERIDAN, J. 2014 Fluid–structure interaction of a square cylinder at different angles of attack. *Journal of Fluid Mechanics* **747**, 688–721.
- ZHAO, J., LO JACONO, D., SHERIDAN, J., HOURIGAN, K. & THOMPSON, M. C. 2018*b* Experimental investigation of in-line flow-induced vibration of a rotating cylinder. *Journal of Fluid Mechanics* **847**, 664–699.
- ZHAO, MING 2013 Flow induced vibration of two rigidly coupled circular cylinders in tandem and side-by-side arrangements at a low reynolds number of 150. *Physics of Fluids* **25** (12), 123601.